Acta Oceanol. Sin., 2021, Vol. 40, No. 1, P. 33–42
https://doi.org/10.1007/s13131-021-1716-3
http://www.hyxb.org.cn
E-mail: hyxbe@263.net

Characterization of sea ice and its snow cover in the Arctic Pacific sector during the summer of 2016

Qing Ji[1, 2], Ying Liu[3], Xiaoping Pang[1, 2, 3], Yue Pan[3], Xi Zhao[1, 2*]
[1] Chinese Antarctic Center of Surveying and Mapping, Wuhan University, Wuhan 430079, China
[2] Key Laboratory of Polar Surveying and Mapping, Ministry of Natural Resources, Wuhan 430079, China
[3] School of Resource and Environmental Sciences, Wuhan University, Wuhan 430079, China

Received 24 April 2020; accepted 26 May 2020

Abstract

A comprehensive analysis of sea ice and its snow cover during the summer in the Arctic Pacific sector was conducted using the observations recorded during the 7th Chinese National Arctic Research Expedition (CHIANRE-2016) and the satellite-derived parameters of the melt pond fraction (MPF) and snow grain size (SGS) from MODIS data. The results show that there were many low-concentration ice areas in the south of 78°N, while the ice concentration and thickness increased significantly with the latitude above the north of 78°N during CHIANRE-2016. The average MPF presented a trend of increasing in June and then decreasing in early September for 2016. The average snow depth on sea ice increased with latitude in the Arctic Pacific sector. We found a widely developed depth hoar layer in the snow stratigraphic profiles. The average SGS generally increased from June to early August and then decreased from August to September in 2016, and two valley values appeared during this period due to snowfall incidents.

Key words: sea ice, snow cover, melt pond fraction, snow grain size, Arctic Pacific sector

Citation: Ji Qing, Liu Ying, Pang Xiaoping, Pan Yue, Zhao Xi. 2021. Characterization of sea ice and its snow cover in the Arctic Pacific sector during the summer of 2016. Acta Oceanologica Sinica, 40(1): 33–42, doi: 10.1007/s13131-021-1716-3

1 Introduction

Arctic sea ice has declined rapidly, as substantiated by the reduction in the extent and thickness of sea ice, loss of multi-year ice coverage and intensification of snow melting on sea ice (Kwok and Rothrock, 2009; Comiso, 2012; Laxon et al., 2013; Xia et al., 2014). Sea ice provides excellent thermal insulation for heat exchange between the ocean and the atmosphere (Teleti and Luis, 2013). Snow on Arctic sea ice can obstruct the absorption of solar radiation by the upper layer of sea ice, relieve the intense melting of sea ice in the summer, and play a significant role in maintaining the mass balance and energy transmission (Grenfell and Maykut, 1977; Sturm et al., 2013). Therefore, analyzing the characterization of Arctic sea ice and its snow cover would benefit understanding of the Earth's radiation and the energy transfer process.

Field observations (including ship-based observations and ice-station observations) provide a valuable dataset for understanding Arctic sea ice and its surface snow variations on a small scale. Ship-based observations can provide the general characteristics of the sea ice concentration and ice thickness from visual interpretations given by the observer on the ship, while ice-station observations focus on the snow and ice interaction process with atmosphere and seawater (Dou et al., 2012). Based on field observation data, Warren et al. (1999) studied the surface characteristics of Arctic sea ice. Additionally, Webster et al. (2014) discussed the variations of snow depth on Arctic sea ice according to snow data measured by the BROMEX project. Based on the field data acquired in the Arctic Expedition Project N-ICE2015, Rösel et al. (2018) explored the changes of sea ice and its snow in the Arctic Atlantic sector from the winter to spring melt period. In China, the field observational data used to study the characteristics of Arctic sea ice and snow are mainly from the Chinese National Arctic Research Expedition (CHINARE). Xiao et al. (1997) analyzed the characteristics of sea ice and snow stratigraphy in the central Arctic based on the first Chinese National Arctic Research Expedition. Moreover, Dou et al. (2012) presented the spatial distribution characteristics of snow cover in the central Arctic Ocean from the field observational data of the 3rd Chinese National Arctic Research Expedition. Additionally, Sun et al. (2017) studied the distribution characteristics of sea ice thickness using the data from ice-station measurements recorded during the 7th Chinese National Arctic Research Expedition.

Satellite remote sensing data could obtain large-scale and long-term information on Arctic sea ice and snow parameters. The melt pond fraction (MPF) on the surface of sea ice during summer is one of the main factors affecting the variability in surface albedo over the ice cover (Tschudi et al., 2008). For information on MPF on a large scale, the representative method is retrieved from optical remote sensing data (Rösel et al., 2012; Istomina et al., 2015; Yackel et al., 2018). The snow grain size (SGS) is another important parameter affecting the radiation balance of snow and ice (Zege et al., 2008). The core idea of the SGS

Foundation item: The National Key Research and Development Program of China under contract No. 2016YFC1402704; the National Natural Science Foundation of China under contract No. 42076235; the Special Fund for High Resolution Images Surveying and Mapping Application System under contract No. 42-Y30B04-9001-19/21.
*Corresponding author, E-mail: xi.zhao@whu.edu.cn

retrieval method based on remote sensing is to establish the relationship between SGS and the optical spectrum. Commonly used models include the Wiscombe Warren (WW) Model (Wiscombe and Warren, 1980), the discrete ordinates radiative transfer (DISORT) model (Nolin and Dozier, 1993) and the analytical asymptotic radiative transfer (AART) model (Zege et al., 2008; Carlsen et al., 2017).

Based on field observations and remote sensing retrievals, a comprehensive analysis of the overall characteristics of Arctic sea ice and snow, as well as the spatio-temporal characteristics of specific indication parameters, can help better understand the changes of Arctic sea ice and snow, and provide a reference for research on the relationship between sea ice, snow, and climate change. In this context, we selected the Arctic Pacific sector as a case study area, which is the main area of the Chinese National Arctic Research Expeditions, and analyzed the field observations of sea ice and snow recorded during the 7th Chinese National Arctic Research Expedition. Meanwhile, the parameters of MPF and SGS were retrieved from MODIS data in the Arctic Pacific sector during the summer of 2016. Finally, we conducted a comprehensive analysis of field observations and remote sensing retrievals to characterize sea ice and its snow cover at both local and regional scales in the Arctic Pacific sector.

2 Data

2.1 *Field observation data*

The 7th Chinese National Arctic Research Expedition (CHINARE- 2016) was conducted in the Arctic Pacific sector from July to September in 2016. The R/V *Xuelong* entered the Arctic sea ice area on July 25 and then sailed along the northbound route, reached the long-term ice station on August 7, and started to sail southward on August 15. The ship route in the Arctic Pacific Sector with the location of ice stations is illustrated in Fig. 1. The Arctic Pacific sector (168°E–144°W) is the main area of the Chinese National Arctic Research Expeditions, and a significant area of seasonal warming and rapidly decreasing sea ice during summer (Nghiem et al., 2007; Maslanik et al., 2011; Frey et al., 2014).

This study used ship-based and station-based observational data from CHINARE-2016 to study the characterization of sea ice and snow at a local scale. The ship-based observations were conducted along the expedition route. The sea ice concentration, ice thickness, ice ridge fraction, MPF, snow depth, and other parameters were recorded within a radius of 1 km according to the Arctic ship-based sea ice standardization tool (ASSIST) protocol. Six short-term and one long-term ice station fieldwork investigations were completed during CHINARE-2016. The physical parameters of snow on sea ice including the snow depth, water content, density, snow stratification, and SGS, were measured and recorded in snow pits.

On August 8, August 17 and August 20 in 2016, we conducted spectral reflectance measurements at the long-term ice station (82°47′N, 162°47′W), SICE05 short-term ice station (79°56′N, 179°21′W) and SICE06 short-term ice station (76°19′N, 179°36′E) (Fig. 1). A total of 87 measurements covering the different surface types of bare ice, snow-covered ice, melt pond, and seawater were recorded using a portable multi-spectral radiometer

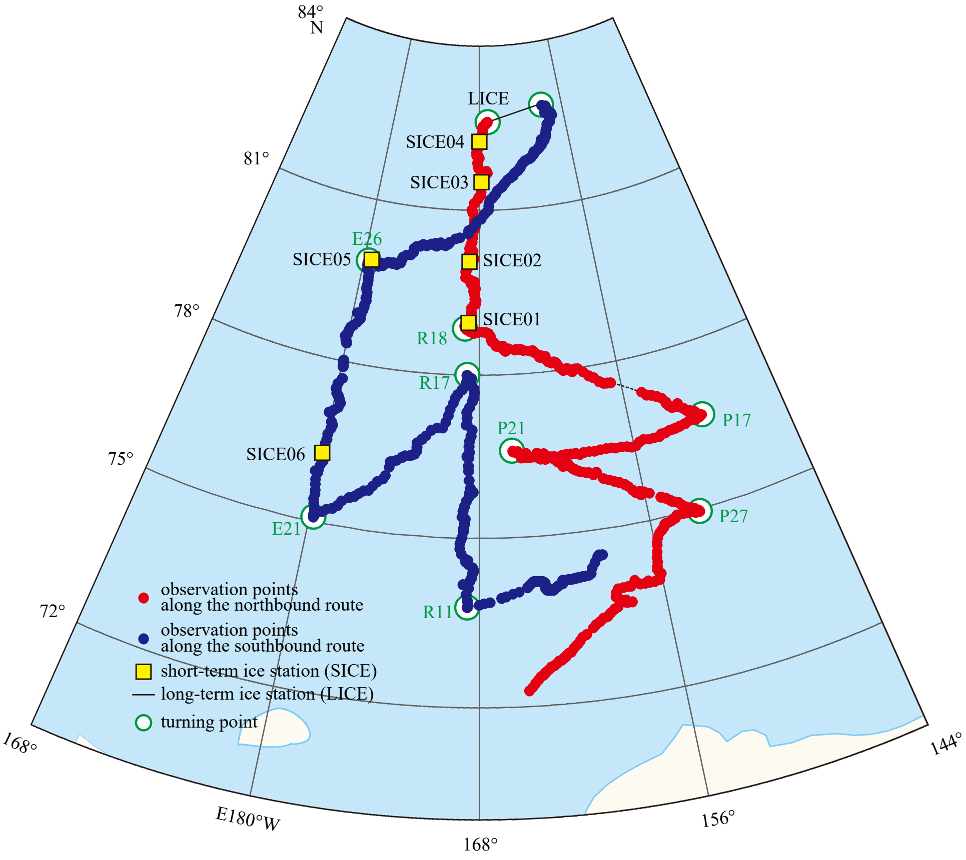

Fig. 1. Distribution of ship-based observations and ice stations in the Arctic Pacific sector during the 7th Chinese National Arctic Research Expedition (CHIANRE-2016).

(MSR) produced by the US CROPSCAN company. Each measurement contained only one pure surface type, with a sensor footprint of 1 m^2. To compare the measured data with the data obtained from the satellite remote sensing sensor, spectral measurements were conducted at 10:00–13:00 local time in the natural state. Meanwhile, these sampling points were located far away from the R/V *Xuelong*, and there were no obstacles. We obtained the average spectral reflectance value for different surface types through multiple measurements with the sampling points distributed as evenly as possible at each ice station to reduce the measurement error and improve the spatial representation.

2.2 *MODIS albedo data*

We used MODIS albedo data to retrieve the MPF and SGS in the Arctic Pacific sector during the summer of 2016. Surface albedo data originated from MODIS product (MOD09A1), which are synthetic data of the 8-d surface reflectance from Band 1 to Band 7 at a 500 m resolution. The MOD09A1 data from June 1 to September 28 of 2016 were acquired from NASA (https://search.earthdata.nasa.gov/search?q=MOD09A1%20V006).

2.3 *Auxiliary data*

In this study, we extracted sea ice pixels with ice concentrations greater than 15% from the AMSR2 sea ice concentration data and calculated the MPF within these ice pixels. AMSR2 sea ice concentration data with a spatial resolution of 3.125 km were obtained from the University of Bremen (https://seaice.uni-bremen.de/data/).

3 Methods

3.1 *Data preprocessing*

Figure 2 shows the workflow of this study. To facilitate subsequent processing and analysis, the collected data were transformed into the same Arctic Polar Stereoscopic Projection and GeoTIFF data format. The ship-based and station-based ice-snow observed data were collocated and averaged to MODIS pixels. We then clipped all of the data using the extracted sea-ice area and the unified defined mask between 168°E–144°W and north of 70°N (the study area of the Arctic Pacific sector).

3.2 *MPF retrieval method*

Based on the mixed pixel model proposed by Fetterer and Untersteiner (1998), Tschudi et al. (2008) took the measured spectral reflectance as the input to solve linear equations with a known reflectance of pixels and surface types, and then calculated the area ratios of different surface types in the Chukchi Sea of the Arctic.

This investigation took the *in-situ* measured spectral reflectance data obtained from CHINARE-2016 as input parameters to solve the linear equations for the distribution of MPF in the Arctic Pacific sector. The linear equations are as follows:

$$A_{\mathrm{W}} r_{\mathrm{W}} (\lambda_1) + A_{\mathrm{M}} r_{\mathrm{M}} (\lambda_1) + A_{\mathrm{I}} r_{\mathrm{I}} (\lambda_1) = R (\lambda_1), \tag{1}$$

$$A_{\mathrm{W}} r_{\mathrm{W}} (\lambda_2) + A_{\mathrm{M}} r_{\mathrm{M}} (\lambda_2) + A_{\mathrm{I}} r_{\mathrm{I}} (\lambda_2) = R (\lambda_2), \tag{2}$$

$$A_{\mathrm{W}} r_{\mathrm{W}} (\lambda_3) + A_{\mathrm{M}} r_{\mathrm{M}} (\lambda_3) + A_{\mathrm{I}} r_{\mathrm{I}} (\lambda_3) = R (\lambda_3), \tag{3}$$

$$A_{\mathrm{W}} + A_{\mathrm{M}} + A_{\mathrm{I}} = 1, \tag{4}$$

where $R(\lambda_k)$ corresponds to the reflectivity of the MODIS pixel in Band k (k =1, 2, 3), which can be acquired from MOD09A1 surface albedo data; A is the coverage of each surface type (W: seawater, M: melt pond, I: sea ice and snow) in each pixel; A_{W}, A_{M}, and A_{I} are the area ratio of open water, melt pond, and sea ice cover on each pixel, respectively; $r(\lambda_k)$ represents the spectral reflectance of each surface type in Band k (k =1, 2, 3), which was obtained from CHINARE-2016 (Section 2.1). Table 1 shows the measured mean spectral reflectance values of each surface type corresponding to MODIS for MPF retrieval.

These linear equations have three unknowns (A_{W}, A_{M}, and A_{I}), which need to be solved using a least square method. A_{W}, A_{M}, and A_{I} should be between 0 and 1, which is the constraint condi-

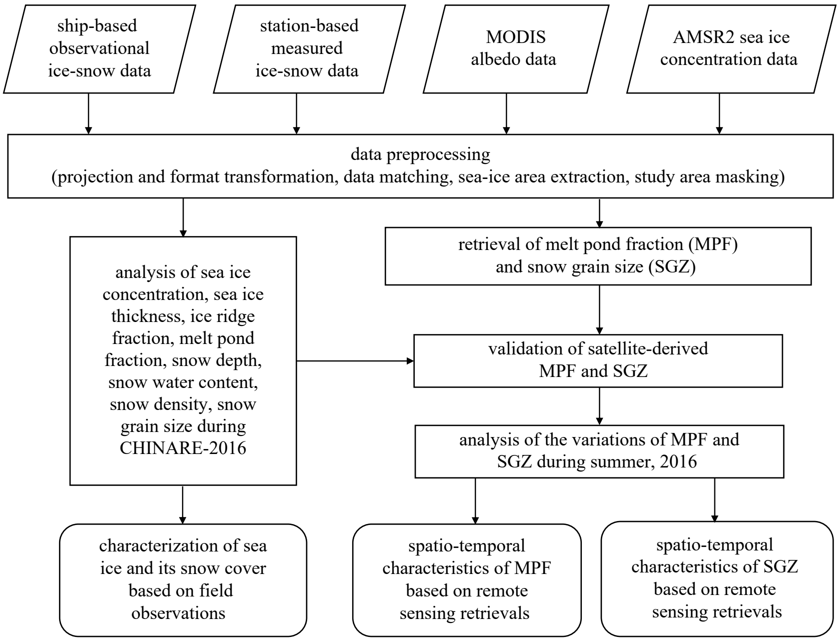

Fig. 2. The workflow of this study.

Table 1. Mean spectral reflectance resulting from multiple measurements for different surface types during CHINARE-2016

Band k	Spectral range/nm	Melt pond r_M	Ice and snow r_I	Open water r_W
1	620–670	0.21	0.78	0.07
2	841–876	0.13	0.65	0.02
3	459–479	0.28	0.84	0.08

tion of solving linear equations with the least squares method. As MPF is defined as the ratio of the melt pond area to the whole sea ice area, it could be obtained by the following equation.

$$MPF = A_M (1 - A_W), \tag{5}$$

3.3 *SGS retrieval method*

In this study, SGS was retrieved using the method of the AART model proposed by Lyapustin et al. (2009). This method considers snow as a non-homogeneous medium, and the snow grain size (d) determined by the absorption Band λ_1 and λ_2:

$$d = \frac{\lambda_5}{4\pi x_5 A^2}\ln^2\left(\frac{\alpha_1}{\alpha_5}\right), \tag{6}$$

where α_1 is the albedo of MODIS Band 1 with λ_1=0.649 9 μm; α_5 is the albedo of MODIS Band 5 with λ_5=1.241 9 μm. The imaginary part (x_5) of the complex refractive ice index corresponding to Band 5 is 1.20e^{-5}. A is the shape factor, whose value depends on the shape of snow grains, and can be expressed as follows:

$$A(\mu_0, \mu, \varphi) = K(1 + 2\mu_0)(1 + 2\mu)/R_0(\mu_0, \mu, \varphi), \tag{7}$$

where K=0.66, and R_0 can be acquired from the lookup table given by Suttles (1988). μ_0, μ and φ represent the solar zenith angle, observation zenith angle, and relative azimuth angle, respectively, which can be acquired from MODIS data. Since this algorithm is only limited in the condition that the solar zenith angle SZA<78°, the pixel with SZA⩾78° is therefore set as a null value. To obtain accurate SGS values, it is necessary to remove invalid values in the study area using a snow cover mask. The snow mask can be calculated by the normalized difference snow index (NDSI), defined as follows:

$$\text{NDSI} = (\rho_4 - \rho_6)/(\rho_4 + \rho_6), \tag{8}$$

where ρ_4 and ρ_6 represent the reflectivity of MODIS Band 4 and Band 6, respectively. The pixel with NDSI⩾0.4, $\rho_2 > 0.11$, and $\rho_4 \geqslant 0.1$ is recognized as a snow pixel.

4 Results

4.1 *Characterization of sea ice and its snow cover based on field observations*

There were many low-concentration sea ice areas in the south of 78°N in the study area during CHINARE-2016 (Fig. 3). The sea ice concentration and ice thickness increased significantly with the latitude above the north of 78°N. Near 81°N, the sea ice thickness decreased, MPF increased, and the size of ice floe increased. There were numerous small ice ridges in the marginal ice zones, which led to an increase in the ice thickness in these zones. Along the northbound route, the MPF was generally higher, with a higher sea ice concentration and thicker ice thickness compared to the southbound route.

Figure 4 shows the average snow depth variation with latitude from 729 ship-based observations during CHINARE-2016. We found that the distribution of snow depth on sea ice in the Arctic Pacific sector in summer increased as the latitude increased from south to north. The average snow depth was 53 mm and the maximum was 300 mm.

The physical characteristics of snow on sea ice in each ice station during CHIANRE-2016 are presented in Table 2. The average snow density at short-term ice stations was 0.272 g/cm^3, and that of long-term ice stations was 0.306 g/cm^3, which are higher than the snow density in August reported by Warren et al. (1999). This change could be explained by the accelerated loss of Arctic sea ice and increasing water content in snow during summer in recent years. As the depth increases, the snow stratification from the snow surface to the bottom displays in the following order: new snow, wind crust, young snow, depth hoar, refreezing course snow, wet snow, and infiltrated-congelation ice. We found that a depth hoar layer was widely developed in the snow, accounting for 40%–60% of the total snow. The snow equivalent grain size

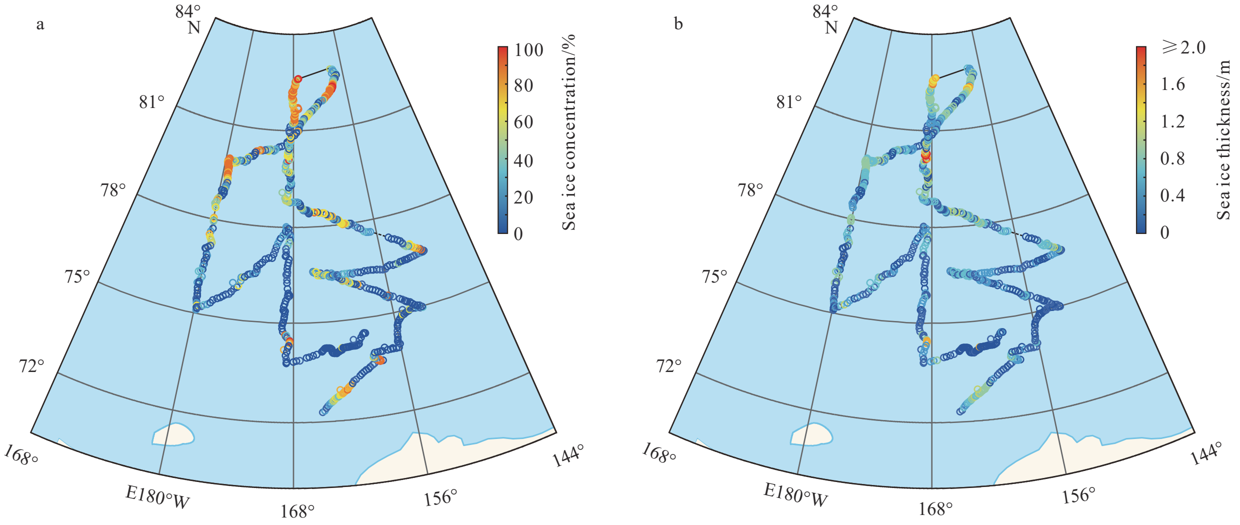

Fig. 3.

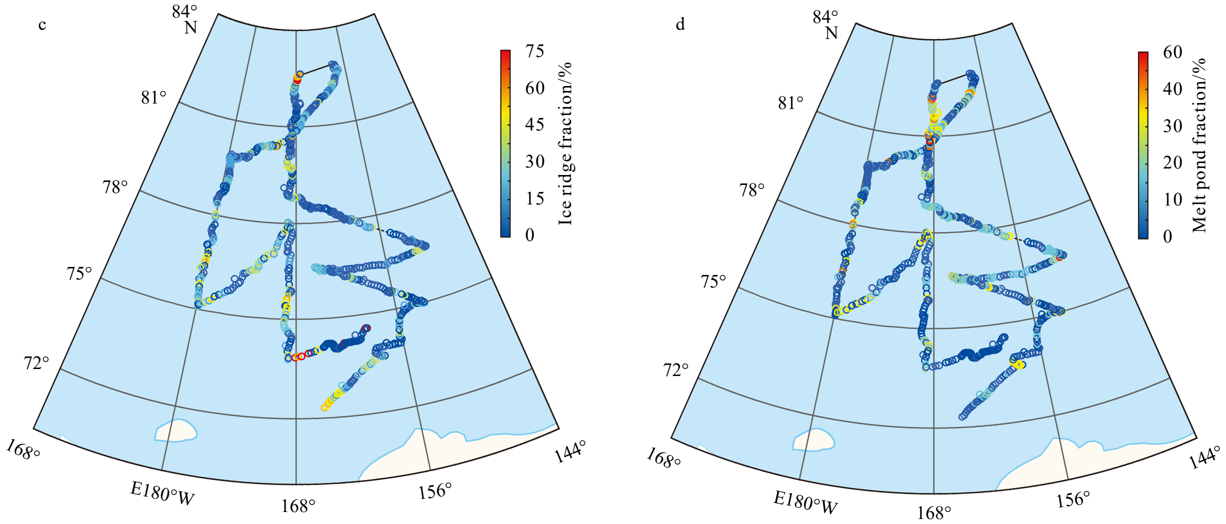

Fig. 3. Spatial distribution of the sea ice concentration (a), sea ice thickness (b), ice ridge fraction (c), and melt pond fraction (d) observed along the R/V *Xuelong* route during CHINARE-2016.

was small on the surface and large at the bottom along with the snow stratigraphic profiles.

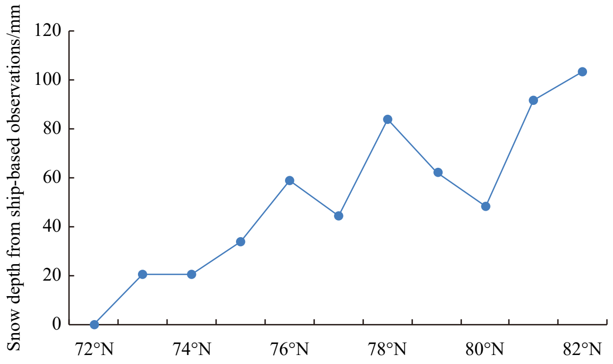

Fig. 4. Snow depth variations with latitude based on ship-based observations during CHINARE-2016.

4.2 *Spatio-temporal characteristics of MPF based on remote sensing retrievals*

To validate MODIS-retrieved MPF in the Arctic Pacific sector (MODIS-MPF), the ship-based observed MPF (OBS-MPF) data from July 25 to August 7 and August 15 to August 25 during CHINARE-2016 were averaged to the matching MODIS pixels and compared to the MODIS-MPF with the same date (Fig. 5). The average bias between MODIS-MPF and OBS-MPF was –0.67%, and –0.79% (–0.50%) for the northbound (southbound) route, respectively, which indicates that MPF retrieved from MODIS is a promising method for obtaining acceptable information on MPF in the Arctic Pacific sector. It should be noted that the scale effect between the MODIS albedo data and *in-situ* measurement data used in the MODIS-derived MPF algorithm could cause errors of the retrieved MPF.

The variations of the 8-d average MPF retrieved from MODIS in the Arctic Pacific sector are plotted in Fig. 6. In the summer of 2016, the average MPF in the Arctic Pacific sector increased first

Table 2. Statistics of snow physical parameters recorded at each ice station during CHIANRE-2016

Ice station	Average water content/%	Average density /(g·cm^{-3})	Description of snow layer and snow grain size		
			Snow layer	Snow type	Equivalent grain size/μm
SICE01	3.61	0.367	bottom layer (2 cm)	depth hoar (coarse firn)	1 128
			middle layer (6 cm)	new snow (circle firn)	685
			surface layer (2 cm)	wind crust (metamorphic snow shell)	978
SICE02	2.09	0.368	bottom layer (5 cm)	depth hoar (coarse firn)	896
			surface layer (8 cm)	new snow (firn)	569
SICE03	4.12	0.385	bottom layer (6 cm)	depth hoar (coarse firn)	1 896
			surface layer (7 cm)	new snow (firn)	1 222
SICE04	4.31	0.306	bottom layer (3 cm)	depth hoar (coarse firn)	1 156
			surface layer (4 cm)	new snow (firn)	1 057
LICE	3.86	0.437	bottom layer (10 cm)	depth hoar (coarse firn)	1 581
			middle layer (14 cm)	new snow (circle firn)	723
			surface layer (2 cm)	new snow	742
SICE05	1.76	0.296	bottom layer (6 cm)	depth hoar (coarse firn)	3 060
			surface layer (1 cm)	wind crust (metamorphic snow shell)	1 935
SICE06	1.901	0.389	bottom layer (20 cm)	depth hoar (coarse firn)	–
			surface layer (2 cm)	wind crust (metamorphic snow shell)	–

Note: – means no data.

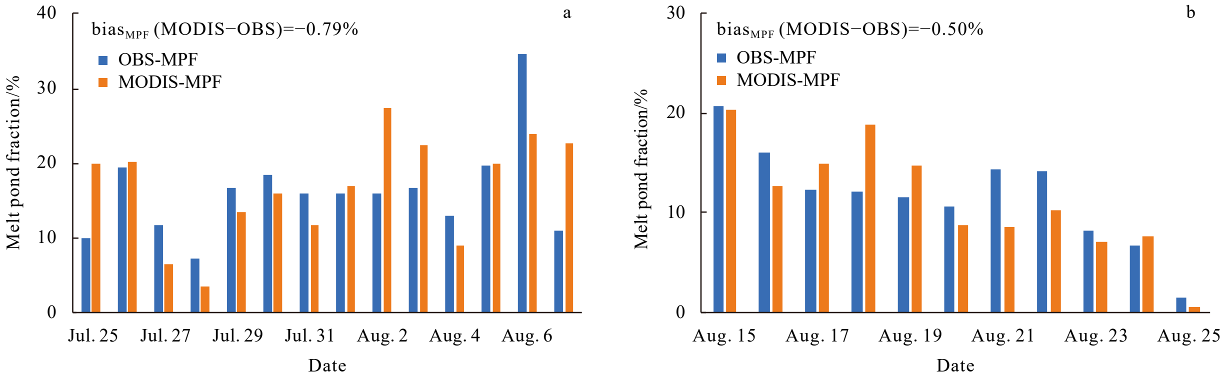

Fig. 5. Comparison of MODIS-derived melt pond fraction (MPF) and ship-based observed MPF during CHINARE-2016: Northbound route (a) and southbound route (b).

and then decreased from June to early September, arriving at a maximum of 25% in early July. The decrease of MPF in August was mainly caused by the drainage of the melting pond. In late September, the melt pond on the multi-year ice was refrozen. However, since new ice began to form, the MPF in the new ice area increased (Shokr and Sinha, 2015). As a result, the average MPF increased slightly in late September.

Figure 7 shows the spatial variations of MPF in the Arctic Pacific sector from the beginning of June to the end of September 2016. The MPF in the low-latitude study area reached about 13% in early June and rose to 20% at the end of June. Meanwhile, the MPF in the high-latitude area was less than 10% in early June and maintained a gradual growth throughout June. In July, ice melt accelerated. The low-latitude area maintained a high MPF (25%–35%), while the value in the high-latitude area increased rapidly in early July. In August, sea ice loss achieved its maximum, and open water increased rapidly. The MPF in the low-latitude areas increased from 30% to 40%, whereas it did not change significantly in the high-latitude areas, ranging from 15% to 20%. The melting period ended in September when new ice began to form in the high-latitude area.

Figure 8 shows the satellite-derived average MPF in the Arctic Pacific sector along the latitude from June 1 to September 28 in 2016. At the end of June, the average MPF reached a high value

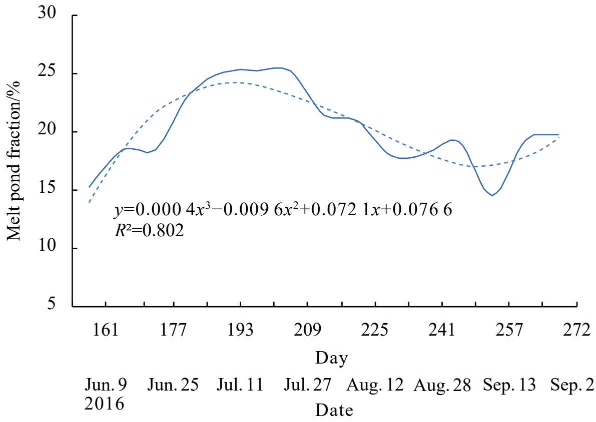

Fig. 6. Variation of the average melt pond fraction (solid line) in the Arctic Pacific sector from June to September in 2016. The dashed line represents the variation trend fitted by cubic polynomial.

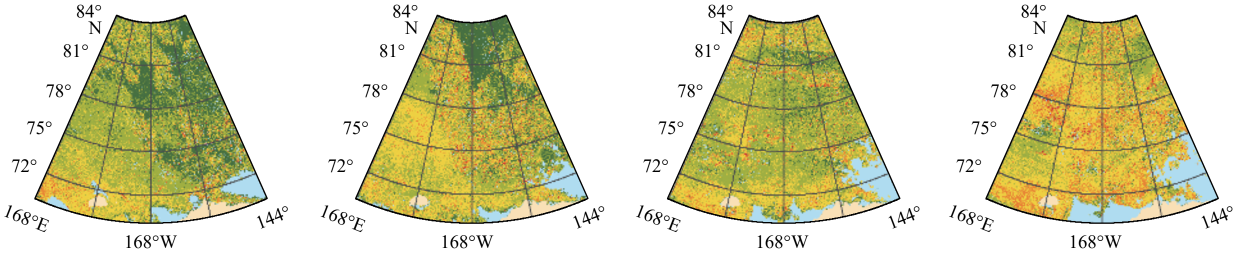

a. Day 153–160 (Jun. 1–Jun. 8)
b. Day 161–168 (Jun. 9–Jun. 16)
c. Day 169–176 (Jun. 17–Jun. 24)
d. Day 177–184 (Jun. 25–Jul. 2)

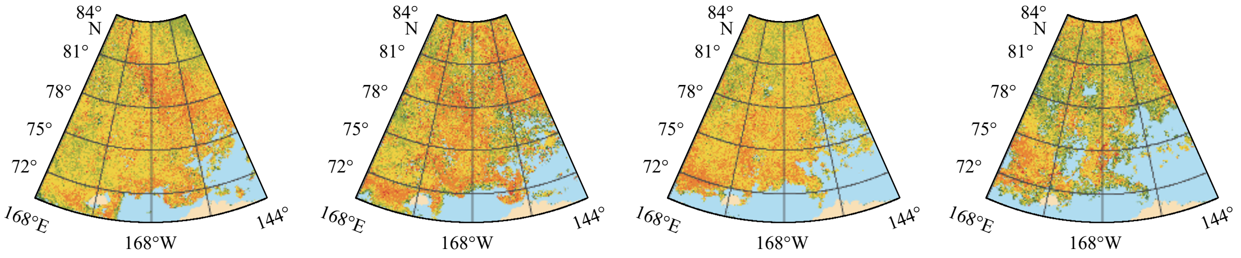

e. Day 185–192 (Jul. 3–Jul. 10)
f. Day 193–200 (Jul. 11–Jul. 18)
g. Day 201–208 (Jul. 19–Jul. 26)
h. Day 209–216 (Jul. 27–Aug. 3)

Fig. 7.

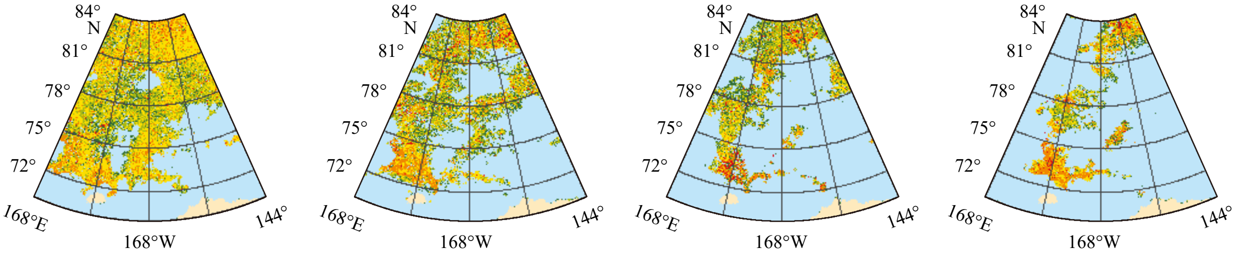

i. Day 217–224 (Aug. 4–Aug. 11) j. Day 225–232 (Aug. 12–Aug. 19) k. Day 233–240 (Aug. 20–Aug. 27) l. Day 241–248 (Aug. 28–Sep. 4)

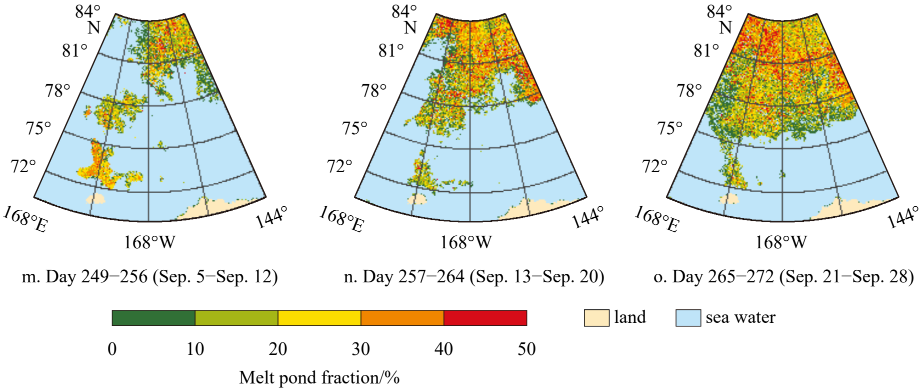

m. Day 249–256 (Sep. 5–Sep. 12) n. Day 257–264 (Sep. 13–Sep. 20) o. Day 265–272 (Sep. 21–Sep. 28)

Fig. 7. Spatial distribution of the melt pond fraction in the Arctic Pacific sector from June to September in 2016.

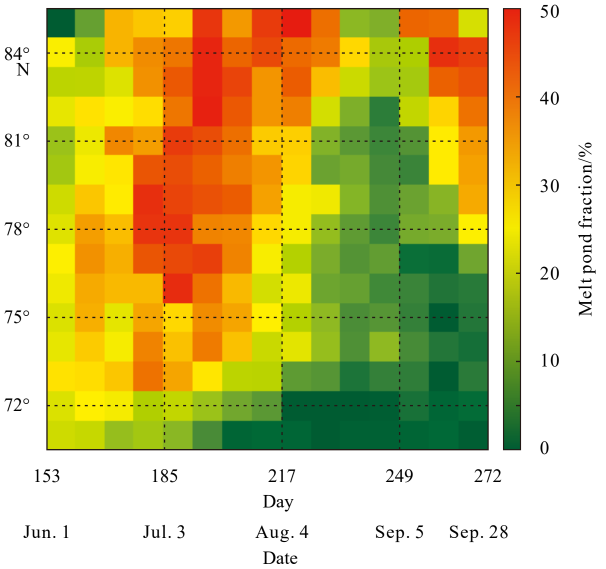

Fig. 8. The average melt pond fraction along the latitude in the Arctic Pacific sector from June to September in 2016.

of 25%–30%, mainly distributed between 76°N and 79°N. The high MPF area gradually moved northward with time, and the maximum was found in the latitude region between 76°N and 84°N from the beginning of July to mid-July.

4.3 *Spatio-temporal characteristics of SGS based on remote sensing retrievals*

We used the average SGS of surface snow layer measured at each ice-station during CHINARE-2016 to validate the matching MODIS-derived SGS according to the *in-situ* measurement location and time (Fig. 9). There is a significant linear relationship

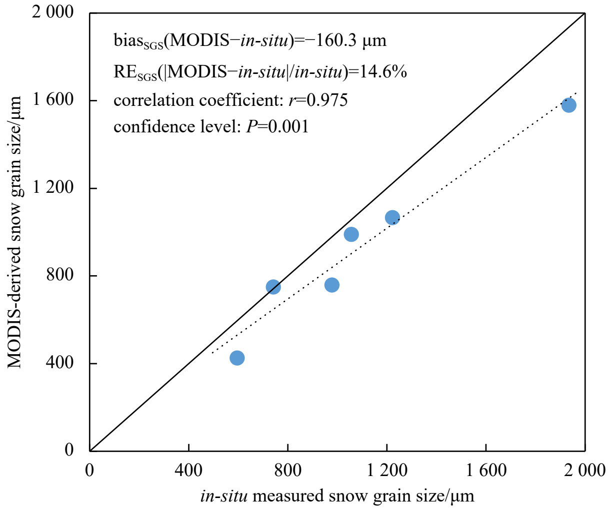

Fig. 9. Comparison of MODIS-derived snow grain size (SGS) and station-based SGS measured during CHINARE-2016. The solid line is the one-to-one fitting line, and the dotted line is the regression line of MODIS-derived SGS to *in-situ* measured SGS. The blue dots are the average SGS of surface snow layer measured at ice stations matched MODIS-derived SGS according to the in-situ measurement location and time.

between MODIS-derived SGS and *in-situ* measured SGS. The average relative error (RE_{SGS}) between MODIS-derived SGS and *in-situ* measured SGS was 14.6%, indicating that SGS retrieved from MOIDS is an acceptable method for obtaining large-scale SGS information. The SGS retrieved from MODIS presented a slightly lower value than the actual SGS, mainly because MODIS could misrecognize the thin cloudy area as cloudless pixels, resulting in underestimation of the value of SGS (Intrieri et al., 2002).

Figure 10 shows the variations of the 8-d average SGS in the Arctic Pacific sector from June to September in 2016. The average SGS generally increased from June to early August and then decreased from August to September. There were two valleys between July 27 and August 20, which were likely due to snowfall events. Wiebe et al. (2013) mentioned that the occurrence of snowfall events will lead to a sudden decrease in SGZ. During CHINARE-2016, snowfall events were observed between July 29 and August 1, and also on August 15, 17, and 20, respectively, coinciding with the occurrence time of these two valleys.

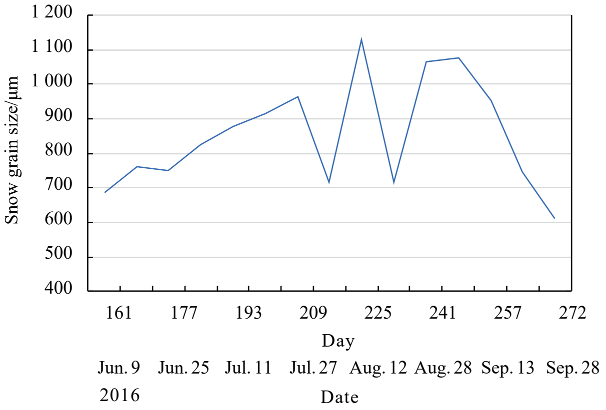

Fig. 10. Variation of the average snow grain size in the Arctic Pacific sector from June to September in 2016.

The spatial variations of SGS in the Arctic Pacific sector from the beginning of June to the end of September in 2016 are plotted in Fig. 11. In early June, the high values of SGS were mainly distributed in the low-latitude area in the southwestern part of the sector. In late June, they were distributed in the high-latitude area. SGS reached its first peak in mid-July and then gradually decreased in late July. In general, the value of SGS was high from early August to early September, except for the days between August 12 and 19. From September 13 to 28, the SGS in the low-latitude region exhibited a decreasing trend.

5 Conclusions

In this study, the characterization of sea ice and its snow cover in the Arctic Pacific sector during CHINARE-2016 was summarized based on ship-based and station-based observations, and the spatio-temporal variations of the MPF and SGS were analyzed based on remote sensing retrievals.

In the summer of 2016, there were many low-concentration sea ice areas in the south of 78°N in the Arctic Pacific sector, and many small ice ridges existed in the marginal ice zones. The sea ice concentration and thickness increased significantly with the latitude above the north of 78°N.

The snow depth on sea ice in the Arctic Pacific sector during CHINARE-2016 was increasingly fluctuating with latitude from south to north. The average snow density was higher than that in previous publications. A depth hoar layer was widely developed in the snow layer, accounting for 40%–60% of the total snow.

The average MPF in the Arctic Pacific sector during the sum-

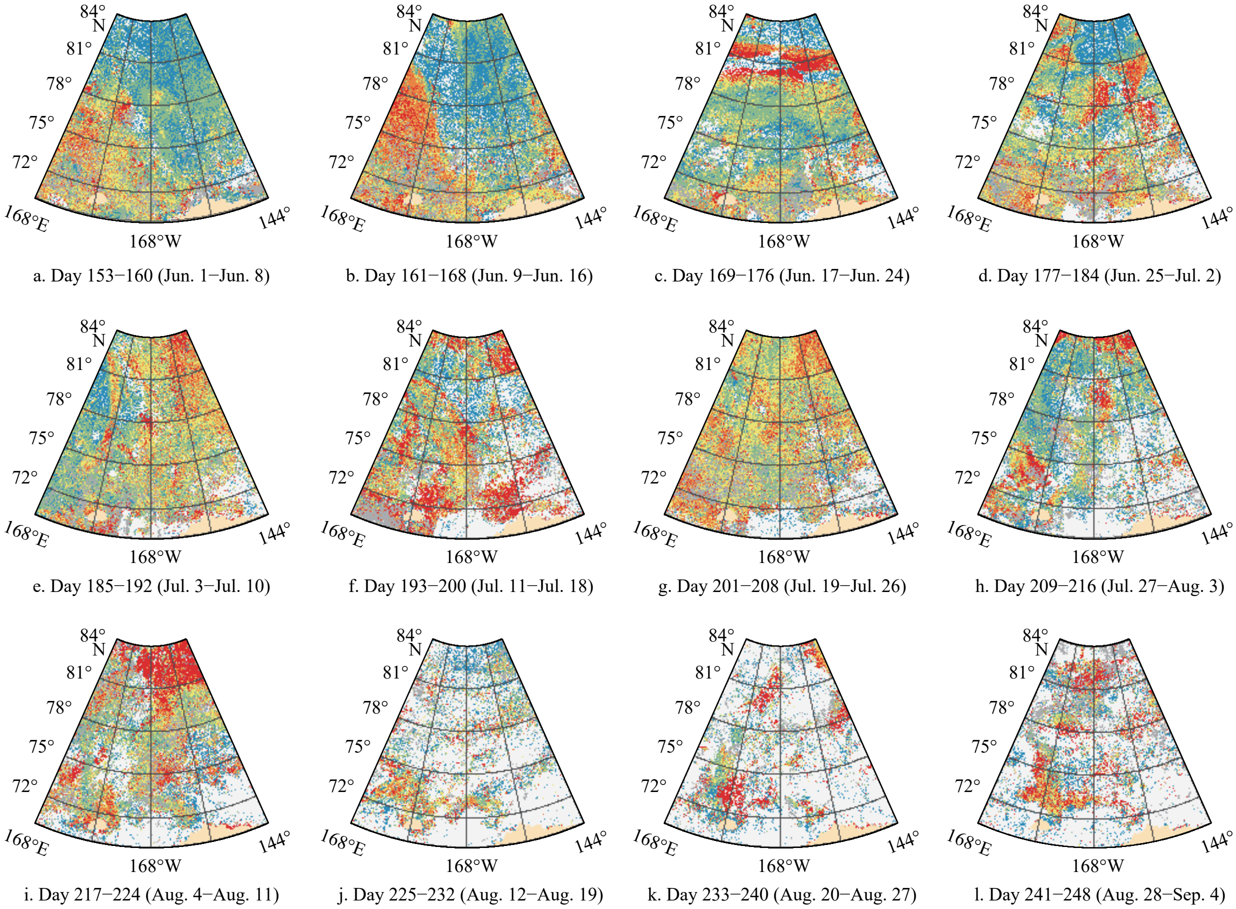

a. Day 153–160 (Jun. 1–Jun. 8)
b. Day 161–168 (Jun. 9–Jun. 16)
c. Day 169–176 (Jun. 17–Jun. 24)
d. Day 177–184 (Jun. 25–Jul. 2)
e. Day 185–192 (Jul. 3–Jul. 10)
f. Day 193–200 (Jul. 11–Jul. 18)
g. Day 201–208 (Jul. 19–Jul. 26)
h. Day 209–216 (Jul. 27–Aug. 3)
i. Day 217–224 (Aug. 4–Aug. 11)
j. Day 225–232 (Aug. 12–Aug. 19)
k. Day 233–240 (Aug. 20–Aug. 27)
l. Day 241–248 (Aug. 28–Sep. 4)

Fig. 11.

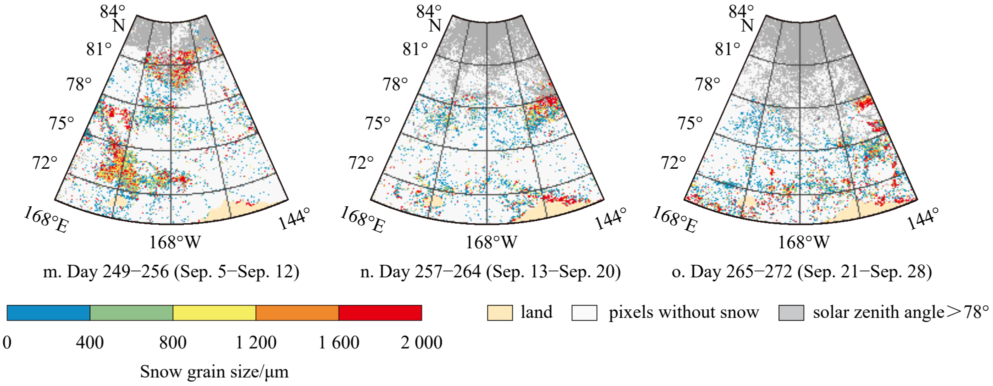

m. Day 249–256 (Sep. 5–Sep. 12)   n. Day 257–264 (Sep. 13–Sep. 20)   o. Day 265–272 (Sep. 21–Sep. 28)

Fig. 11. Spatial distribution of snow grain size in the Arctic Pacific sector from June to September in 2016.

mer of 2016 presented a trend of increasing first and then decreasing from June to early September and increased slightly in late September due to the formation of new ice. The high MPF area gradually moved northward with time, and the maximum was found in the latitude region between 76°N and 84°N from the beginning of July to mid-July.

The average SGS generally increased from June to early August and then decreased from August to September in 2016. In early June, the high values of SGS were mainly distributed in the low-latitude area southwest of the Arctic Pacific sector, while in late June, they were distributed in the high-latitude area. In general, the value of SGS was relatively high from early July to early September.

Acknowledgements

We thank the members of the 7th Chinese National Arctic Research Expedition and the crews of R/V *Xuelong* for their assistance during the ship-based and station-based ice and snow observations.

References

Carlsen T, Birnbaum G, Ehrlich A, et al. 2017. Comparison of different methods to retrieve optical-equivalent snow grain size in central Antarctica. The Cryosphere, 11(6): 2727–2741, doi: 10.5194/tc-11-2727-2017

Comiso J C. 2012. Large decadal decline of the Arctic multiyear ice cover. Journal of Climate, 25(4): 1176–1193, doi: 10.1175/JCLI-D-11-00113.1

Dou Tingfeng, Xiao Cunde, Guo Rui, et al. 2012. Analysis on features of snow cover on the Arctic sea ice in summer of 2008. Journal of Glaciology and Geocryology (in Chinese), 34(1): 43–48

Fetterer F, Untersteiner N. 1998. Observations of melt ponds on Arctic sea ice. Journal of Geophysical Research: Oceans, 103(C11): 24821–24835, doi: 10.1029/98JC02034

Frey K E, Maslanik J A, Kinney J C, et al. 2014. Recent variability in sea ice cover, age, and thickness in the Pacific Arctic region. In: Grebmeier J M, Maslowski W, eds. The Pacific Arctic Region: Ecosystem Status and Trends in a Rapidly Changing Environment. Dordrecht: Springer, 31-63

Grenfell T C, Maykut G A. 1977. The optical properties of ice and snow in the Arctic Basin. Journal of Glaciology, 18(80): 445–463, doi: 10.1017/S0022143000021122

Intrieri J M, Shupe M D, Uttal T, et al. 2002. An annual cycle of Arctic cloud characteristics observed by radar and LIDAR at SHEBA. Journal of Geophysical Research: Oceans, 107(C10): SHE 5-1–SHE 5-15

Istomina L, Heygster G, Huntemann M, et al. 2015. Melt pond fraction and spectral sea ice albedo retrieval from MERIS data-Part 2: Case studies and trends of sea ice albedo and melt ponds in the Arctic for years 2002–2011. The Cryosphere, 9(4): 1567–1578, doi: 10.5194/tc-9-1567-2015

Kwok R, Rothrock D A. 2009. Decline in Arctic sea ice thickness from submarine and ICESat records: 1958–2008. Geophysical Research Letters, 36(15): L15501

Laxon S W, Giles K A, Ridout A L, et al. 2013. CryoSat-2 estimates of Arctic sea ice thickness and volume. Geophysical Research Letters, 40(4): 732–737, doi: 10.1002/grl.50193

Lyapustin A, Tedesco M, Wang Y, et al. 2009. Retrieval of snow grain size over Greenland from MODIS. Remote Sensing of Environment, 113: 1976–1987, doi: 10.1016/j.rse.2009.05.008

Maslanik J, Stroeve J, Fowler C, et al. 2011. Distribution and trends in Arctic sea ice age through spring 2011. Geophysical Research Letters, 38(13): L13502

Nghiem S V, Rigor I G, Perovich D K, et al. 2007. Rapid reduction of Arctic perennial sea ice. Geophysical Research Letters, 34(19): L19504, doi: 10.1029/2007GL031138

Nolin A W, Dozier J. 1993. Estimating snow grain size using AVIRIS data. Remote Sensing of Environment, 44(2–3): 231–238, doi: 10.1016/0034-4257(93)90018-S

Rösel A, Itkin P, King J, et al. 2018. Thin sea ice, thick snow, and widespread negative freeboard observed during N-ICE2015 north of Svalbard. Journal of Geophysical Research: Oceans, 123(2): 1156–1176, doi: 10.1002/2017JC012865

Rösel A, Kaleschke L, Birnbaum G. 2012. Melt ponds on Arctic sea ice determined from MODIS satellite data using an artificial neural network. The Cryosphere, 6(2): 431–446, doi: 10.5194/tc-6-431-2012

Shokr M, Sinha N. 2015. Sea Ice: Physics and Remote Sensing. Washington, DC: American Geophysical Union

Sturm M, Morris K, Massom R. 2013. The winter snow cover of the West Antarctic pack ice: Its spatial and temporal variability. In: Jeffries M O, ed. Antarctic Sea Ice: Physical Processes, Interactions and Variability. Washington, DC: American Geophysical Union, 1–18

Suttles J T, Green R N, Minis P, et al. 1988. Angular radiation models for earth-atmosphere system. Hampton, Virginia, USA: NASA Langley Research Center

Sun Xiaoyu, Shen Hui, Li Chunhua, et al. 2017. Arctic sea ice observation and characteristic analysis based on the seventh National Arctic Research expedition in summer 2016. Marine Forecasts (in Chinese), 34(4): 11–19

Teleti P R, Luis A J. 2013. Sea ice observations in Polar regions: Evolution of technologies in remote sensing. International Journal of Geosciences, 4(7): 1031–1050, doi: 10.4236/ijg.2013.47097

Tschudi M A, Maslanik J A, Perovich D K. 2008. Derivation of melt pond coverage on Arctic sea ice using MODIS observations. Remote Sensing of Environment, 112(5): 2605–2614, doi: 10.1016/j.rse.2007.12.009

Warren S G, Rigor I G, Untersteiner N, et al. 1999. Snow depth on Arctic sea ice. Journal of Climate, 12(6): 1814–1829, doi: 10.1175/1520-0442(1999)012<1814:SDOASI>2.0.CO;2

Webster M A, Rigor I G, Nghiem S V, et al. 2014. Interdecadal changes in snow depth on Arctic Sea Ice. Journal of Geophysical Research: Oceans, 119(8): 5395–5406, doi: 10.1002/2014JC009985

Wiebe H, Heygster G, Zege E, et al. 2013. Snow grain size retrieval SGSP from optical satellite data: validation with ground measurements and detection of snow fall events. Remote Sensing of Environment, 128: 11–20, doi: 10.1016/j.rse.2012.09.007

Wiscombe W J, Warren S G. 1980. A model for the spectral albedo of snow. I: Pure snow. Journal of the Atmospheric Sciences, 37(12): 2712–2733, doi: 10.1175/1520-0469(1980)037<2712:AMFTSA>2.0.CO;2

Xia Wentao, Xie Hongjie, Ke Changqing. 2014. Assessing trend and variation of Arctic sea-ice extent during 1979–2012 from a latitude perspective of ice edge. Polar Research, 33(1): 21249, doi: 10.3402/polar.v33.21249

Xiao Cunde, Qin Dahe, Ren Jiawen. 1997. The feature of sea ice cover, snow distribution and its densification in the central Arctica. Scientia Geographica Sinica (in Chinese), 17(4): 289–296

Yackel J J, Nandan V, Mahmud M, et al. 2018. A spectral mixture analysis approach to quantify Arctic first-year sea ice melt pond fraction using QuickBird and MODIS reflectance data. Remote Sensing of Environment, 204: 704–716, doi: 10.1016/j.rse.2017.09.030

Zege E, Katsev I, Malinka A, et al. 2008. New algorithm to retrieve the effective snow grain size and pollution amount from satellite data. Annals of Glaciology, 49: 139–144, doi: 10.3189/172756408787815004